

RESEARCH ARTICLE

Homogenized modeling methodology for 18650 lithium-ion battery module under large deformation

Liang Tang*, Jinjie Zhang, Pengle Cheng

School of Engineering, Beijing Forestry University, Beijing, China

* tang-l04@mails.tsinghua.edu.cn



OPEN ACCESS

Citation: Tang L, Zhang J, Cheng P (2017) Homogenized modeling methodology for 18650 lithium-ion battery module under large deformation. PLoS ONE 12(7): e0181882. <https://doi.org/10.1371/journal.pone.0181882>

Editor: Xiaosong Hu, Chongqing University, CHINA

Received: May 8, 2017

Accepted: July 8, 2017

Published: July 26, 2017

Copyright: © 2017 Tang et al. This is an open access article distributed under the terms of the [Creative Commons Attribution License](https://creativecommons.org/licenses/by/4.0/), which permits unrestricted use, distribution, and reproduction in any medium, provided the original author and source are credited.

Data Availability Statement: All relevant data are within the paper.

Funding: This work is financially supported by the National Science Foundation of China under Grants No. 51605032, the National Science Foundation of Beijing under Grant No. 3174052 and the Fundamental Research Funds for the Central Universities No. 2017ZY31. The funders had no role in study design, data collection and analysis, decision to publish, or preparation of the manuscript.

Competing interests: The authors have declared that no competing interests exist.

Abstract

Effective lithium-ion battery module modeling has become a bottleneck for full-size electric vehicle crash safety numerical simulation. Modeling every single cell in detail would be costly. However, computational accuracy could be lost if the module is modeled by using a simple bulk material or rigid body. To solve this critical engineering problem, a general method to establish a computational homogenized model for the cylindrical battery module is proposed. A single battery cell model is developed and validated through radial compression and bending experiments. To analyze the homogenized mechanical properties of the module, a representative unit cell (RUC) is extracted with the periodic boundary condition applied on it. An elastic–plastic constitutive model is established to describe the computational homogenized model for the module. Two typical packing modes, i.e., cubic dense packing and hexagonal packing for the homogenized equivalent battery module (EBM) model, are targeted for validation compression tests, as well as the models with detailed single cell description. Further, the homogenized EBM model is confirmed to agree reasonably well with the detailed battery module (DBM) model for different packing modes with a length scale of up to 15×15 cells and 12% deformation where the short circuit takes place. The suggested homogenized model for battery module makes way for battery module and pack safety evaluation for full-size electric vehicle crashworthiness analysis.

Introduction

With the strong support from the government [1] and major technology breakthrough for lithium-ion batteries (LIBs) [2, 3], electric vehicles (EVs) have been witnessed to boom over the past recent years [4–6]. The major reason for LIBs to become the primary choice for EVs is due to the combination advantage of high energy/power density, lightweight, and safety [6, 7]. Many research works were conducted on the optimization approach for electrified vehicles to increase cost competitiveness and reduce carbon emissions [6, 8–10]. Additionally, the battery management system plays an important role in maintaining battery lifetime without unduly sacrificing its performance. Some key technologies of battery management system that monitor the unmeasurable internal states of the battery have been extensively studied [11–14].

Battery models such as electrochemical [13], thermal [15], and high-order physics-based model [16] are also used for evaluation of existing charging strategies, estimator and controller development, simulation, and optimization. However, none of these works have considered the mechanical performance of the battery. Because of the inevitable crash or impact for vehicles during traffic accidents, there is a high possibility of internal short-circuit [15], thermal runaway [17], and even explosion [18, 19] for LIBs subjected to external mechanical loading. Thus, the crashworthiness issue of EVs by consideration of LIB safety remains a paramount concern in electric vehicle safety.

In the past years, many pioneering efforts were made to elucidate the mechanical safety behavior of LIBs on multiple length scales, ranging from component material scale to battery pack scale. On the component level, the mechanical properties of the case [20], separator [21], anode, and cathode foils [22] of the cell have been investigated. These results will help to understand the failure mechanism of internal short circuit of lithium-ion battery, but can not characterize the global mechanical behavior of the battery. Many experiments were conducted for the investigation of mechanical behaviors of the battery cells under various loading conditions [20, 23, 24]. The finite element (FE) models were used to understand the mechanical properties and predict extreme cases. Since coating of active material coating and separator are highly porous and soaked in the electrolyte, the detailed modeling including each component and interaction among them is very complicated. Therefore, it is reasonable and acceptable to take jellyroll as a homogeneous material [23, 25, 26]. Furthermore, the dynamic behavior [27] and SOC effect [28] of the battery have been studied and the results suggested that higher SOC leads to higher structure stiffness. In this paper, a computational model of a single cylindrical battery is established and validated based on homogeneous modeling technique.

For battery module and pack, the mechanical safety performance is closely related to sizes and packing modes of the module and modeling every single cell in detail would be costly. Therefore, equivalent homogenized model for the module is fully necessary for many applications such as vehicle level crashworthiness analyses and optimum design. Sahraei et al. [29] used a homogenized crushable foam core to simulate the interior containing battery cells of an idealized battery pack to model the drop test. The battery pack was taken as a linear elastic material in [30] for crash analysis of a conceptual electric vehicle. However, modeling the module by using a simple bulk material would result in sacrificing computational accuracy. Additionally, Lai et al. [31] adopted macro homogenized material models calibrated by the test data to simulate the punch test of a small-scale module specimen. Nevertheless, it is very difficult to directly measure the integrated mechanical properties of the battery module.

This paper responds to the challenge by extracting a representative unit cell (RUC) with the periodic boundary condition applied on it to analyze the homogenized mechanical properties of the module. An elastic–plastic constitutive model is established to describe the equivalent battery module (EBM) model. Further, a small-scale battery module is tested to compare the mechanical behavior with those obtained from the EBM model and detailed battery module (DBM) model. Upon the satisfactory comparison results, EBM model is further generalized for larger battery modules and different packing modes and the feasibility of the established model is discussed.

Methods

2.1 Computational model of a single cell LIB

Mechanical behavior of a single cell LIB surely dominates that of a battery module. The 18650 LixC6/LiCoO₂ batteries are used in this study, provided by SONY. The main cell geometry and dimensions are provided in Fig 1A. The cylindrical LIB cell is composed of winding

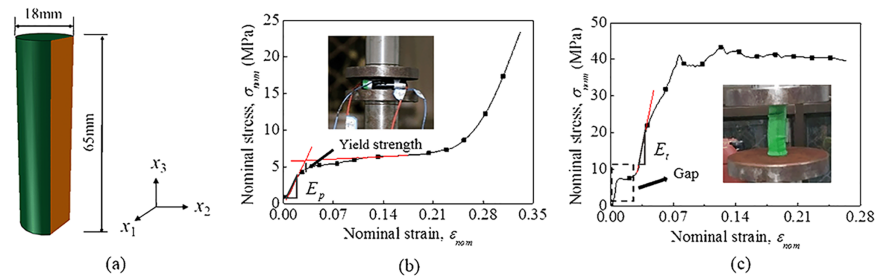


Fig 1. Mechanical behavior of 18650 lithium-ion battery. (a) The 18650 lithium-ion battery. Nominal stress–strain curve of a single LIB under (b) radial compression and (c) axial compression conditions.

<https://doi.org/10.1371/journal.pone.0181882.g001>

cathode, anode, and separator films and encapsulated into a steel can. So it is extremely complicated to simulate each component and interaction among them in detail. Thus, the entire LIB is taken as an orthotropic homogeneous material. For simplicity, the x_1 – x_2 plane that is perpendicular to the axis of the battery is considered as isotropic and a transversely isotropic elastic plastic model has been adopted to express the mechanical properties.

The stress-strain laws for transversely isotropic elasticity are shown as follows:

$$\begin{Bmatrix} \epsilon_{11} \\ \epsilon_{22} \\ \epsilon_{33} \\ \gamma_{12} \\ \gamma_{13} \\ \gamma_{23} \end{Bmatrix} = \begin{bmatrix} 1/E_p & -\nu_p/E_p & -\nu_{tp}/E_t & 0 & 0 & 0 \\ -\nu_p/E_p & 1/E_p & -\nu_{tp}/E_t & 0 & 0 & 0 \\ -\nu_{pt}/E_p & -\nu_{pt}/E_p & 1/E_t & 0 & 0 & 0 \\ 0 & 0 & 0 & 1/G_p & 0 & 0 \\ 0 & 0 & 0 & 0 & 1/G_t & 0 \\ 0 & 0 & 0 & 0 & 0 & 1/G_t \end{bmatrix} \begin{Bmatrix} \sigma_{11} \\ \sigma_{22} \\ \sigma_{33} \\ \sigma_{12} \\ \sigma_{13} \\ \sigma_{23} \end{Bmatrix} \quad (1)$$

where p and t stand for “in-plane” and “transverse,” respectively. Thus, E_p and E_t are Young’s modulus of radial and axial directions, $E_1 = E_2 = E_p$ and $E_3 = E_t$; G_p and G_t are the shear modulus of the corresponding planes, $G_{12} = G_p$ and $G_{13} = G_{23} = G_t$; ν_p , ν_{tp} and ν_{pt} are the Poisson’s ratio, $\nu_{12} = \nu_p$ and $\nu_{13} = \nu_{23} = \nu_{pt}$; and subscripts “1”, “2” and “3” stand for the coordinate system.

The anisotropic yield behavior is modeled through yield stress ratio, R_{ij} , which is applied in Hill’s potential function. The yield stress ratio is defined as follows:

$$R_{ij} = \begin{bmatrix} \frac{\bar{\sigma}_{11}}{\sigma_0} & \frac{\bar{\sigma}_{12}}{\tau_0} & \frac{\bar{\sigma}_{13}}{\tau_0} \\ & \frac{\bar{\sigma}_{22}}{\sigma_0} & \frac{\bar{\sigma}_{23}}{\tau_0} \\ & & \frac{\bar{\sigma}_{33}}{\sigma_0} \end{bmatrix} \quad (2)$$

where each $\bar{\sigma}_{ij}$ is the measured yield stress value; σ_0 is the user-defined reference yield stress set as 5 MPa; $\tau_0 = \sigma_0/\sqrt{3}$.

The plastic-hardening model for the compression is expressed as the form of the Eq. (3) proposed by Greve and Fehrenbach [23]:

$$\sigma = A\epsilon^n + B \quad (3)$$

Table 1. Summary of material properties for a single cell.

Elasticity modulus	Poisson's ratio	Yield stress ratios	Hardening model
$E_p = 260MPa$	$\nu_p = 0.1$	$R_{ij} = \begin{bmatrix} 1.1 & 1.8 & 12 \\ 0 & 1.1 & 12 \\ 0 & 0 & 8.4 \end{bmatrix}$	$A = 19000$
$E_t = 1200MPa$	$\nu_{pt} = 0.08$		$B = 5.83$
$G_p = 118MPa$			$n = 5.9$
$G_t = 500MPa$			

<https://doi.org/10.1371/journal.pone.0181882.t001>

where A and B are the parameters to be determined, σ is the stress, ϵ is the plastic strain, and n is the hardening exponent.

The above developed mechanical model is calibrated through the radial compression and axial compression tests, as shown in Fig 1B and 1C. The compression tests were conducted on INSTRON 8801 platform with a loading rate of 2 mm/min, where the indenter and the bearing were both flats. The force and displacement sensors were set on the indenter. For radial compression, the nominal stress-strain curve can be converted from the load-displacement curve as follows:

$$\sigma_{nom} = \frac{F}{S_c} \tag{4}$$

$$S_c = l_c b_c \tag{5}$$

$$b_c = 2R \arccos\left(\frac{R - s/2}{R}\right) \tag{6}$$

$$\epsilon_{nom} = \frac{s}{2R} \tag{7}$$

where F is the load and S_c stands for the contact area; l_c is the length of the cell and b_c is the contact width; R is the radius of the cell and s is the displacement of the indenter. The radial compressive nominal stress-strain curve distinctly has three stages, as follows: linear region, plateau region, and densification region. The axial modulus is extracted from the second stage of the curve because the cap collapsed during the axial compression test. The parameter values for the mechanical model of a single cell are summarized in Table 1.

To validate the model, the simulations of radial compression and bending were conducted based on the ABAQUS/Explicit platform on which the proposed constitutive model was used. The bending experiment data were cited from open literature and more detailed information could have been referred from another study [26]. The computational model of the 18650 lithium-ion battery cell was composed of eight-node linear brick, reduced integration solid element with the size of 0.8 mm. As illustrated in Fig 2A and 2B, the model can well predict the mechanical behavior of the cell under radial compression and bending loading conditions, where the coefficient of determination $r^2 = 1 - \frac{\sum (y_i - f_i)^2}{\sum (y_i - \bar{y})^2} = 0.97$ (where y_i and f_i are the experimental and simulated data, respectively, and \bar{y} is the average of the experimental data).

2.2 RUC extraction for the battery module

The packing method of cylindrical cells can be treated as a geometrical model, where packing sizes and modes of the module were uniformly defined with b , l , and θ as shown in Fig 3. b and l are the number of cells on each row and column and θ describes the relative position of rows,

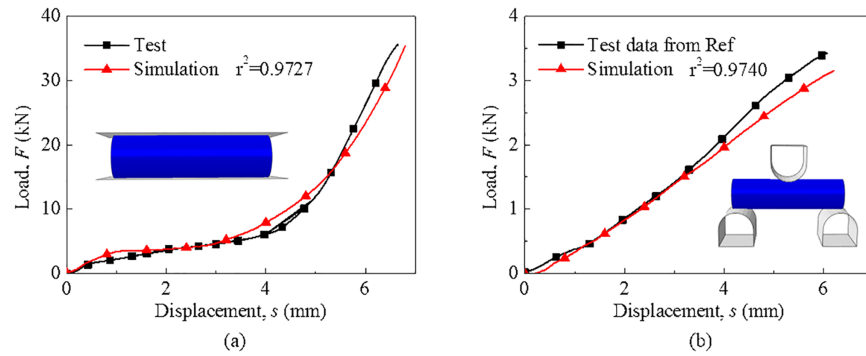


Fig 2. Validation for the computational model of 18650 lithium-ion battery. Mechanical responses from tests and simulations in loading conditions: (a) radial compression and (b) bending.

<https://doi.org/10.1371/journal.pone.0181882.g002>

which varies from $2\pi/3$ to π . The packing density of the module can be expressed as follows:

$$\rho = \frac{\pi bl}{4(b + \cos\frac{\theta}{2})(l\sin\frac{\theta}{2} + 1 - \sin\frac{\theta}{2})} \tag{8}$$

Since the battery module can be regarded as the periodic arrangement of RUCs, RUC of the packing module is extracted. As shown in Fig 2, RUC is related to θ , where the nominal density should be calculated as the following:

$$\rho_{RUC} = \frac{\pi}{4\sin\frac{\theta}{2}} \left(\frac{2\pi}{3} < \theta \leq \pi \right) \tag{9}$$

Naturally, ρ_{RUC} equals the packing density of a module when b and l are regarded as infinite. In this paper, the mechanical properties of RUC are assumed to be equivalent to the properties of the module. When $\theta = \pi$ and $\theta = 2\pi/3$, i.e., cubic dense packing and hexagonal dense packing, the RUC is symmetrical in structure, and the structure of module is stable during compression deformation.

2.3 Computational model for RUC

For a battery module, the length of the cell is sufficiently long relative to its axial deformation, and every cross section of the module perpendicular to the axes of the cell is identical.

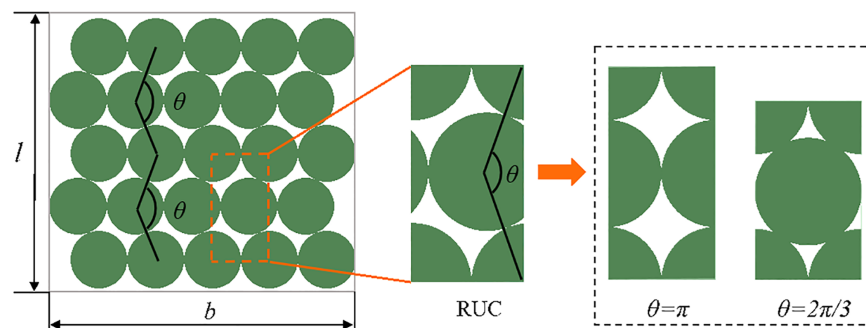


Fig 3. Battery module and extraction of RUC. Diagram of battery module and RUC defined by l , b , and θ and typical RUCs with $\theta = \pi$ and $2\pi/3$.

<https://doi.org/10.1371/journal.pone.0181882.g003>

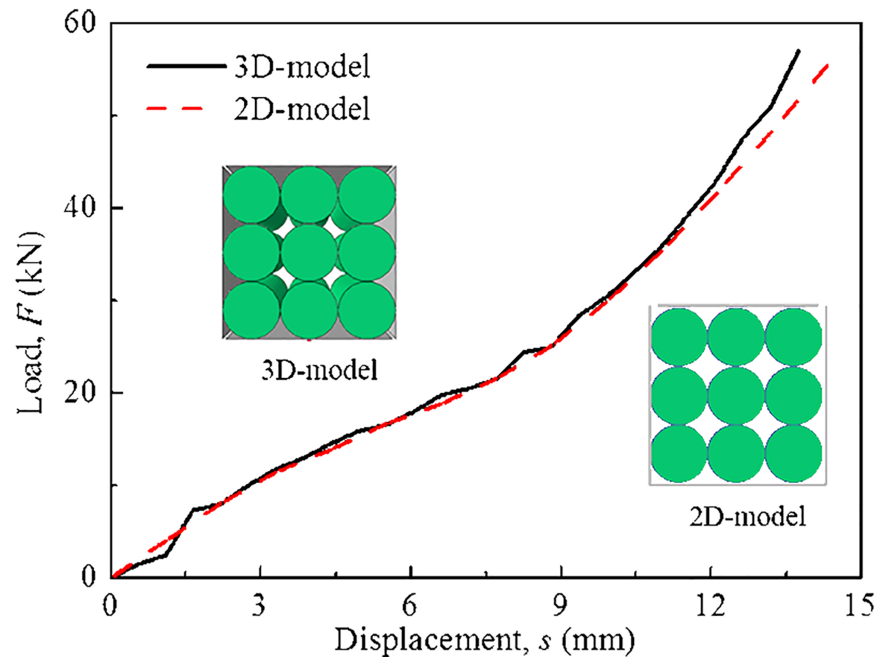


Fig 4. Comparison of 3D and 2D models under constrained compression loading conditions.

<https://doi.org/10.1371/journal.pone.0181882.g004>

Therefore, it is reasonable to be simplified into a two-dimensional plane strain problem. In order to verify the simplification from 3D to 2D, constrained compression simulations using 3D model and 2D model, respectively, were performed, as shown in Fig 4. The results of 2D model and 3D model are almost the same with each other. Then, 2D model is chosen for the next works.

2D model was developed to represent the 3D RUC and the RUC FE model was composed of four-node bilinear quadrilateral plane strain, which reduced integration 2D solid elements with the size of 0.8×0.8 mm. A penalty based contact was set for the contacting parts of adjacent cells by reasonably assuming a friction coefficient of 0.1. To understand the compressive mechanical properties of RUC, a periodic boundary condition that has been investigated in Ref [32–35] was applied to the boundaries of RUC and the boundary equation, as follows:

$$u_i^{j+} - u_i^{j-} = \bar{\epsilon}_{ik} \Delta x_k^j (i, j = 1, 2, 3) \tag{10}$$

where u is the displacement of node, $\bar{\epsilon}_{ik}$ are the average strains, index “j+” means along the positive X_j direction and “j-” means along the negative X_j direction and Δx_k^j are distances between pairs of opposite boundary surfaces. The top and bottom sides were forced and fixed separately to achieve the mechanical properties.

2.4 Homogenized method for battery module modeling

A homogenized method is proposed to replace the detailed modeling method for the battery module. The mechanical properties of the homogenized EBM model can be equivalent to the properties of the RUC model.

Fig 5 shows the true stress–strain curves of RUCs for two typical packing modes during uniaxial compression deformation. The true stress–strain curve could be converted from the

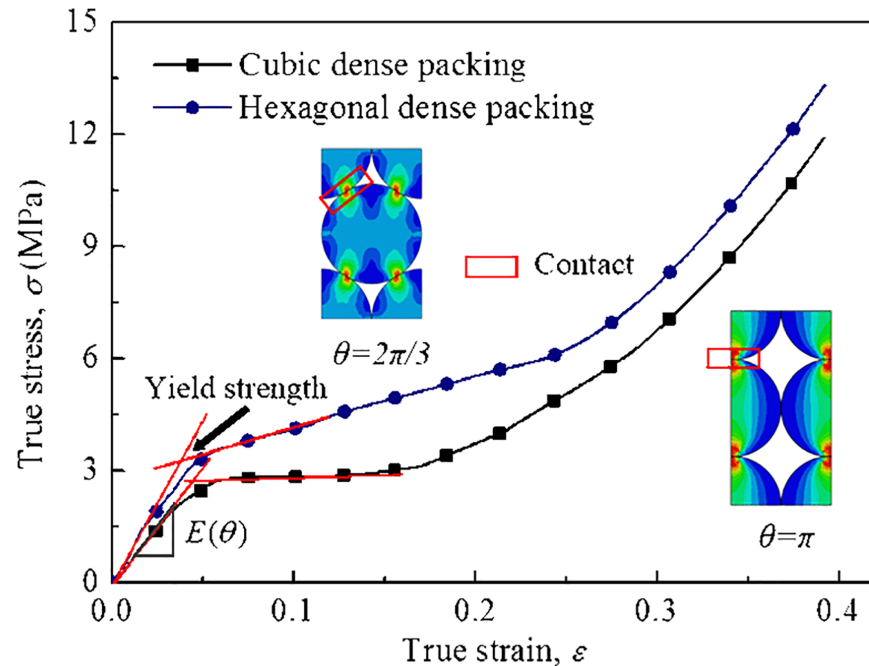


Fig 5. Mechanical properties of RUC. True stress–strain curves of two typical RUCs in uniaxial compression simulation. The plots of deformed RUCs are shown in subplot of the figure.

<https://doi.org/10.1371/journal.pone.0181882.g005>

nominal stress–strain curve as follows:

$$\begin{aligned} \epsilon_{\text{true}} &= \ln(1 + \epsilon_{\text{nom}}) \\ \sigma_{\text{true}} &= \sigma_{\text{nom}}(1 + \epsilon_{\text{nom}}) \end{aligned} \tag{11}$$

where ϵ_{nom} and σ_{nom} can be calculated from the load force and displacement divided by the contact area and the original height of the RUC. The curves first increase linearly to a plateau stage and then increase sharply after the plateau stage. Apparently, there is a difference between the two curves that the stress for hexagonal dense packing is higher than that of cubic dense packing because of its larger density.

An elastic–plastic material model can be used to predict the homogenized EBM behavior. Young’s modulus $E(\theta = \pi)$ and $E(\theta = 2\pi/3)$ are calculated from above true stress–strain curves as 55 and 90 MPa, respectively. The plastic stage of the curves are used as input file of the plastic part of the material model.

2.5 Experiment setups for EBM model verification

To validate the proposed homogenized EBM model, the constrained compression experiments in quasi-static loading condition that commonly occurred during traffic accidents were conducted on INSTRON 8801 platform with a loading rate of 2 mm/min as shown in Fig 6. The battery modules included nine fully discharged battery cells, which are in contact with one another for typical cubic dense packing and hexagonal dense packing. Connection tabs and cooling systems existing in a realistic battery module were neglected. The width and height of the module were within 65 mm in a small size. Moreover, the battery module was restrained by two steel plates with thickness of 20 mm. The distance between the two plates could be adjusted to the size of the module and the plates are fixed by bolts. For reduction of friction

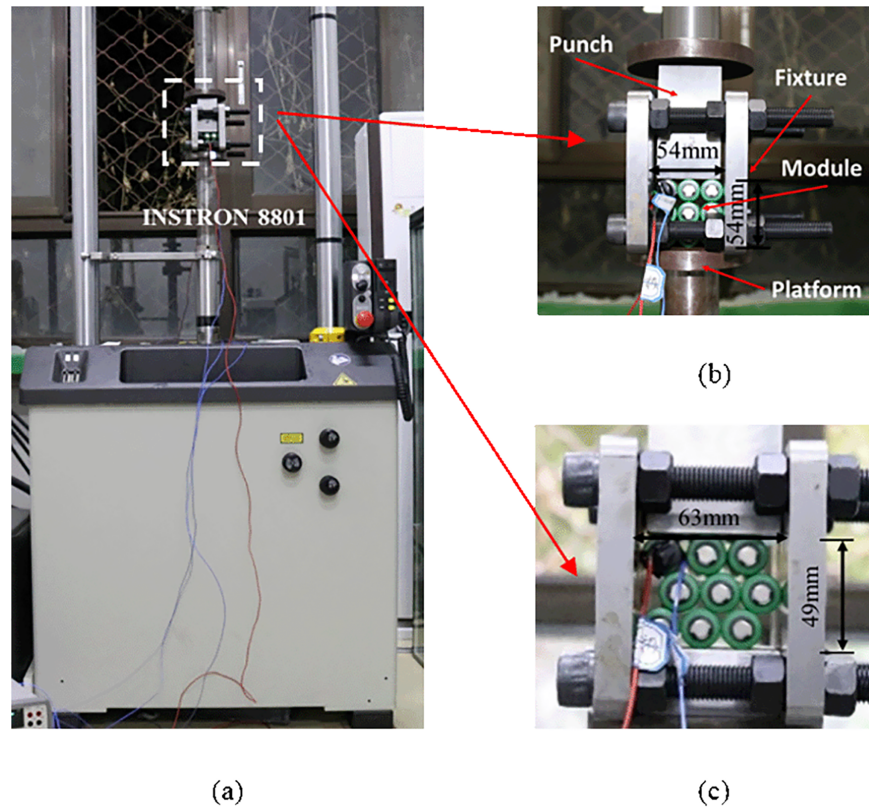


Fig 6. Experiment setups for validation. (a) The setups of compression experiments for the module. Battery module for (b) cubic dense packing and (c) hexagonal dense packing during compression experiment.

<https://doi.org/10.1371/journal.pone.0181882.g006>

effect, the width of load transfer punch is slightly smaller than the distance between the plates. The battery module was compressed by 10 mm, which was about 20% of its height.

Results

Experiments, homogenized EBM model and corresponding DBM model were conducted on the case for the cubic dense packing mode, i.e. $\theta = \pi$. The settings of boundary conditions for both computational models were exactly the same as in the experiment.

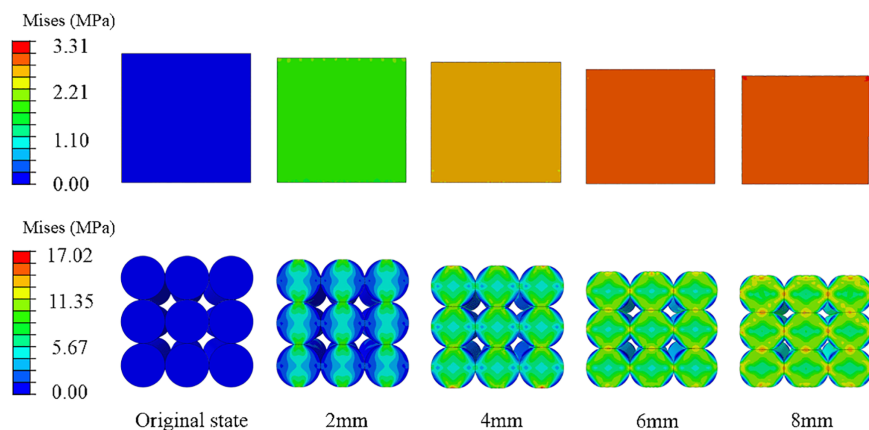


Fig 7. The stress evolution of the module during deformation. Progression of the buildup under constrained compression condition for EBM model (top) and DBM model (bottom).

<https://doi.org/10.1371/journal.pone.0181882.g007>

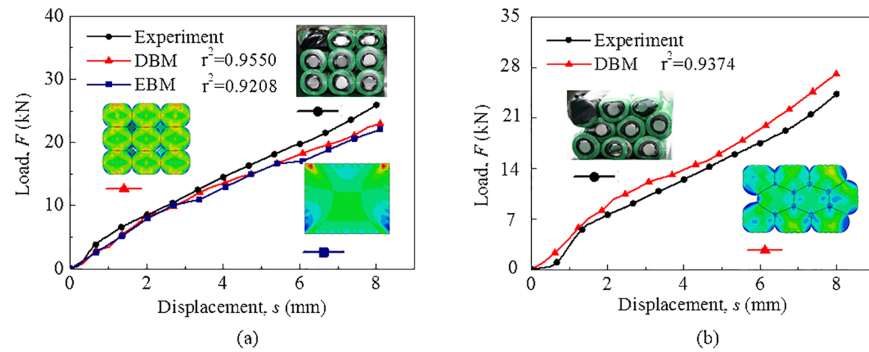


Fig 8. Mechanical responses of the battery module in small size. Comparison of results of the module under constrained compression condition for (a) cubic dense packing and (b) hexagonal dense packing. The plots of deformed modules in the experiment and simulations are shown in the subplot of the figure.

<https://doi.org/10.1371/journal.pone.0181882.g008>

For the EBM computational model, four-node bilinear quadrilateral plane strain, which reduced the integration of 2D solid elements, was used; this was also verified via convergence study. Moreover, the proposed homogenized mechanical properties in Section 2.4 were adopted. For the DBM model, nine single battery cell models were included that developed in Section 2.1. The supporting platform and the indenter were set as discrete rigid. The indenter was designated a certain displacement with quasi-static compressive loading. A penalty-based contact was set for the contacting parts by reasonably assuming a friction coefficient of 0.1.

The stress evolution of the module during deformation is shown in Fig 7. The stress distribution of EBM model is mean, and the corners near the load are under high stress state. For the DBM model, the stress wave spreads from contact area along the load direction to the rest part of the cell, and the stress values of contacting areas of the neighboring cells are higher. In addition, the maximum stress value of the EBM model is smaller than that of DBM model under the same deformation because of larger contact area. It should be noted that, as the deformation increases, the stress growth of the EBM model slows down. As presented in the subsequent section, in the overall mechanical response, the deviation of the load between the EBM model and the DBM model will increase dramatically when the deformation exceeds a certain range. Therefore, the homogenized EBM model can only precisely predict the mechanical behavior of a battery module within a certain deformation range.

Comparison of the mechanical responses of the battery module for cubic dense packing is shown in Fig 8A. The load-displacement curves are close to one another (where $r^2 = 0.92-0.96$), thereby indicating that the EBM model can well predict the integral mechanical behavior of the battery module under constrained compression loading conditions on a small size. It is noted that the EBM model could not distinctively simulate the local mechanical behavior such as contacts between neighboring cells.

Additionally, as illustrated in Fig 8, the DBM model can well reflect the mechanical behavior and deformation of the module for cubic dense packing (where $r^2 = 0.96$) and hexagonal dense packing (where $r^2 = 0.94$), so it could be used as a method to validate the EBM model if it is difficult to conduct an experiment.

Discussions

4.1 Applicability for the battery module under large size

In general, there are more than nine cells in a realistic battery module. Therefore, the applicability of the homogenized modeling method for the module should be validated under large

size. The EBM model and DBM model under different sizes were conducted in constrained compression loading condition for two typical packing modes, i.e., cubic dense packing and hexagonal dense packing. Because the maximum force generated during experiments for the module including nine cells already reached almost 100 kN load limit of the INSTRON 8801, the validation under larger size will be conducted by the DBM model.

For the cubic dense packing mode, the packing density of a module is equivalent to that of corresponding RUC under different sizes. Fig 9 shows the comparisons of mechanical responses between the EBM model and DBM model under different sizes. For observation convenience, the mechanical responses are expressed as the form of load–strain curves and the subscript “ $b \times l$ ” denotes that a number of b and l cells are placed in each row and column, respectively. It is found that there is a good agreement between the EBM model and DBM model under each size (where $r^2 = 0.94\text{--}0.99$), which indicates that the mechanical behavior can be predicted well by this model with length scale up to 15×15 in the range of 15% deformation where the structure of cubic dense packing is stable. When the size reaches a greatly extent, the slight dislocation of individual cells in the module will occur due to deformation of cells, which leads to a load decline.

For the hexagonal dense packing mode, the packing density of a module increases as the increase of its size b and l from Eq. (8). Fig 10 shows the comparisons of mechanical responses between the EBM model and DBM model as well as the packing density of the module under different sizes. It is observed that the difference between the EBM model and DBM model becomes small gradually as the size increases (where r^2 increases from 0.30 to 0.99). Since the effect of size could be eliminated according to the aforementioned result of cubic dense packing, it is reasonable that the EBM model can more precisely describe the module when the density of the module approaches that of its RUC.

When the battery module is taken as a homogenized composite where cells and air are seen as fibers and matrix, respectively, its elastic modulus depends on the volume fraction and elastic property of components according to the composite rule of mixture. Therefore, the elastic

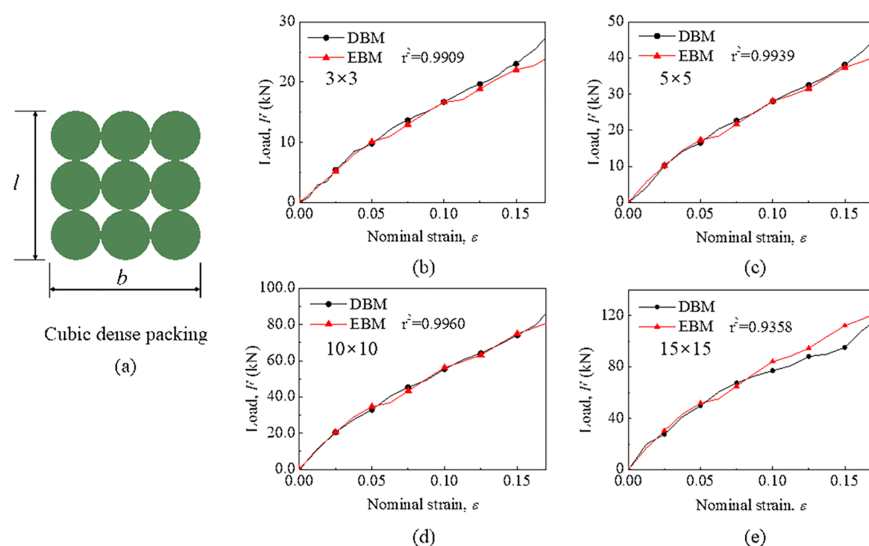


Fig 9. Validation for cubic dense packing under different sizes. (a) Size of cubic dense packing defined by b and l . Comparisons of mechanical responses of the module under different sizes between the EBM model and DBM model where the packing density is constant. The sizes of the module are labeled in each graph.

<https://doi.org/10.1371/journal.pone.0181882.g009>

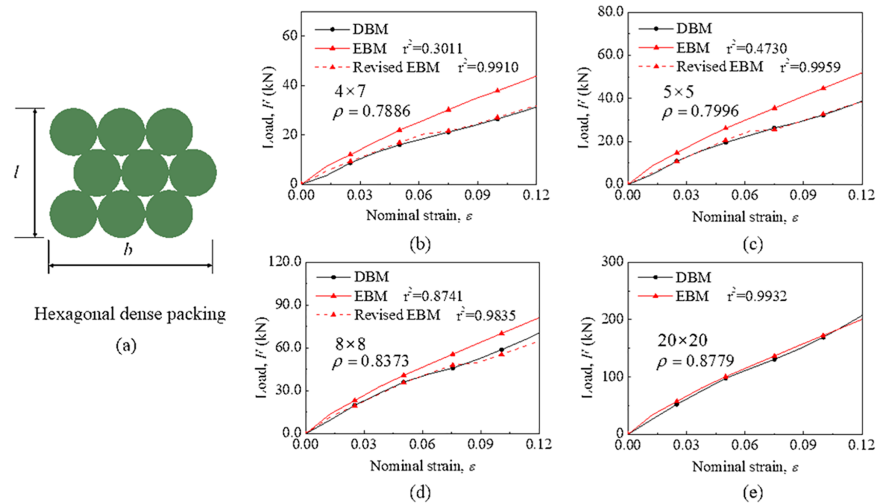


Fig 10. Validation for hexagonal dense packing under different sizes. (a) Size of hexagonal dense packing defined by b and l . Comparisons of mechanical responses of the module under different sizes between the EBM model and DBM model where the packing density is variable. The sizes and densities of the module are labeled in each graph.

<https://doi.org/10.1371/journal.pone.0181882.g010>

modulus of the EBM model can be modified to make this model more accurately describe the module under different sizes. Fig 10 shows that the revised EBM model can predict well the mechanical behavior under different sizes in the range of 12% deformation (where $r^2 = 0.98-0.99$). The ratios of modified elastic modulus E and original modulus $E(\theta = 2\pi/3)$ are shown in Fig 11A and fitted as a function relationship with packing density ρ as follows:

$$\frac{E}{E(\theta = 2\pi/3)} = 1.29\rho^{7.6} + 0.42 \tag{12}$$

As shown in Fig 11B, as predicted by Eq. (12), the EBM model can reflect well the mechanical behavior of the module for hexagonal dense packing under “15 × 15” size with $r^2 = 0.98$.

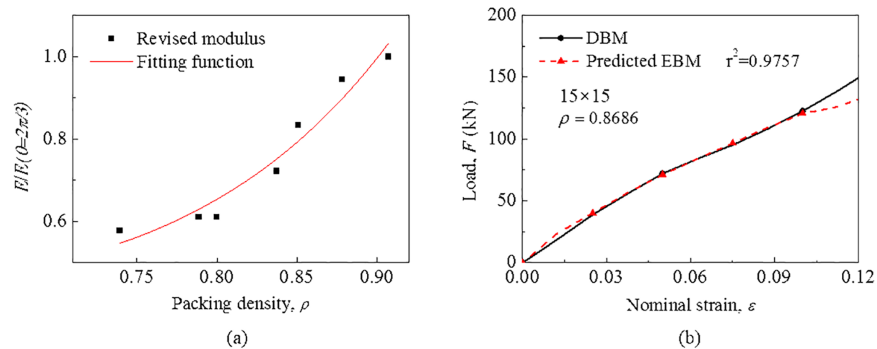


Fig 11. The revised EBM model for hexagonal dense packing. (a) The function relationship with packing density for hexagonal dense packing. (b) Comparison of mechanical responses of the module between the predicted EBM model and DBM model.

<https://doi.org/10.1371/journal.pone.0181882.g011>

4.2 Applicability for different packing modes

Besides aforementioned two typical packing modes where the structure of the module is stable during compression deformation, the cylindrical battery cells can also be arranged for other packing modes, i.e., $2\pi/3 < \theta < \pi$. Fig 12A shows the mechanical behavior of modules with the same size (“10 × 10”) for different packing modes. The load plateau can be observed, which is negligible in the whole compression process. After removing the load plateau, the remainder of the curve is parallel to the curve that describes the module for hexagonal dense packing (the dotted lines represent the remainder of the curves). Evidently, the reason for this phenomenon is that the individual cells in the module overcome the friction to conduct relative motion and tend to form hexagonal dense packing. Thus, the verified EBM model for the hexagonal dense packing mode can be used to predict the mechanical behavior for the asymmetric packing modes, only removing the load plateau stage.

As demonstrated in Fig 12B, when the module fully converts to the hexagonal dense packing mode, assuming the cell was not deformed, the theoretical plateau strain ϵ_p^* can be calculated through the geometrical relationship as follows:

$$\epsilon_p^* = 1 - \frac{\sqrt{3}}{2\sin\frac{\theta}{2}} \tag{13}$$

The equation shows that the length of the load plateau increases with the augment of θ , and that is in accord with what is presented in Fig 12A. In fact, the plateau length is always smaller than the theoretical value because of the limit of size and boundary condition. Fig 12C shows the mechanical responses of the module for $\theta = 5\pi/6$ with variables b and l . It is suggested that

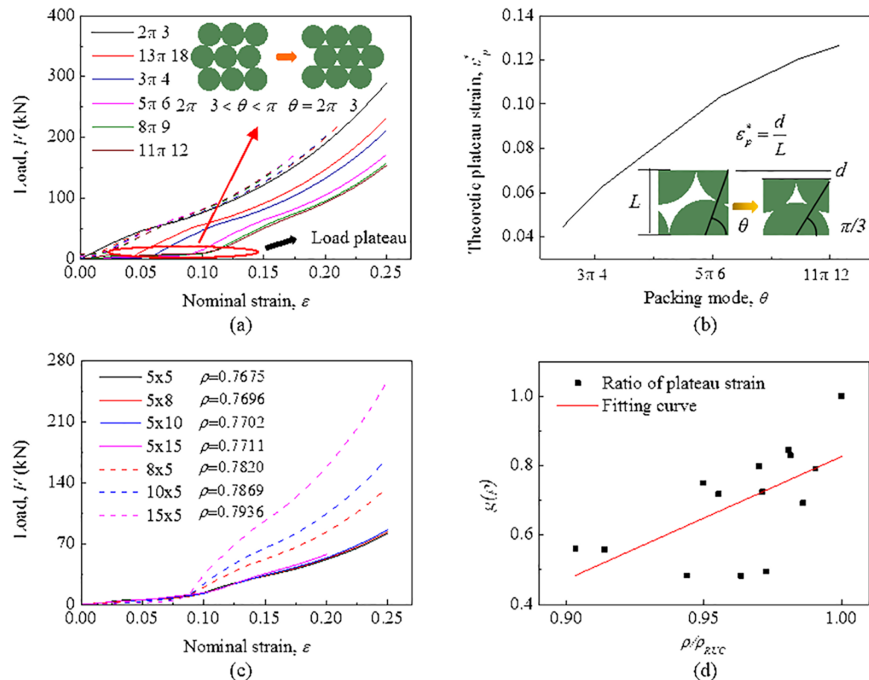


Fig 12. Mechanical behavior of the module for asymmetric packing modes. (a) Mechanical responses of the module with a DBM model for different packing modes when $b = l = 10$. (b) The relationship of theoretical plateau strain and packing mode. (c) Mechanical responses of the module for $\theta = 5\pi/6$ with variables b and l . (d) The fitting function relationship with the ratio of packing density to that of corresponding RUC.

<https://doi.org/10.1371/journal.pone.0181882.g012>

the plateau length hardly depends on the size while closely related to packing density. An empirical formula predicting the length of plateau can be proposed as follows:

$$\epsilon_p = f(\theta, \rho) = \epsilon_p^*(\theta)g(\rho) \tag{14}$$

As shown in Fig 12D, since the range of packing density of a module relies on its packing mode, $g(\rho)$ can be fitted as the following:

$$g(\rho) = 3.54 \frac{\rho}{\rho_{RUC}} - 2.71 \tag{15}$$

where ρ_{RUC} is the density of RUC calculated from Eq. (9) and the ratio ρ/ρ_{RUC} is chosen to eliminate the effect of packing mode.

To validate this model for asymmetric packing modes, two packing forms were chosen with different sizes, modes, and densities, namely, $\theta = 13\pi/18$, where $b = 8$ and $l = 6$, and $\theta = 8\pi/9$, where $b = 7$ and $l = 8$. Fig 13 shows the mechanical responses neglecting the load plateau of the module, and it is observed that there is a satisfactory agreement with the EBM model for hexagonal packing mode under the same size (where $r^2 = 0.93-0.98$), suggesting the accuracy and capability of the EBM model in predicting the mechanical behavior of the battery module.

Concluding remarks

Correctly predicting the mechanical behavior of the module subjected to mechanical loading is critical to understanding the mechanical integrity of the battery pack and ensuring full vehicle crash safety. In this paper, a general method to establish the computational homogenized EBM model is proposed. For the convenience of study, we uniformly defined the packing size and mode of the module. Moreover, the RUC was extracted from the module and the periodic

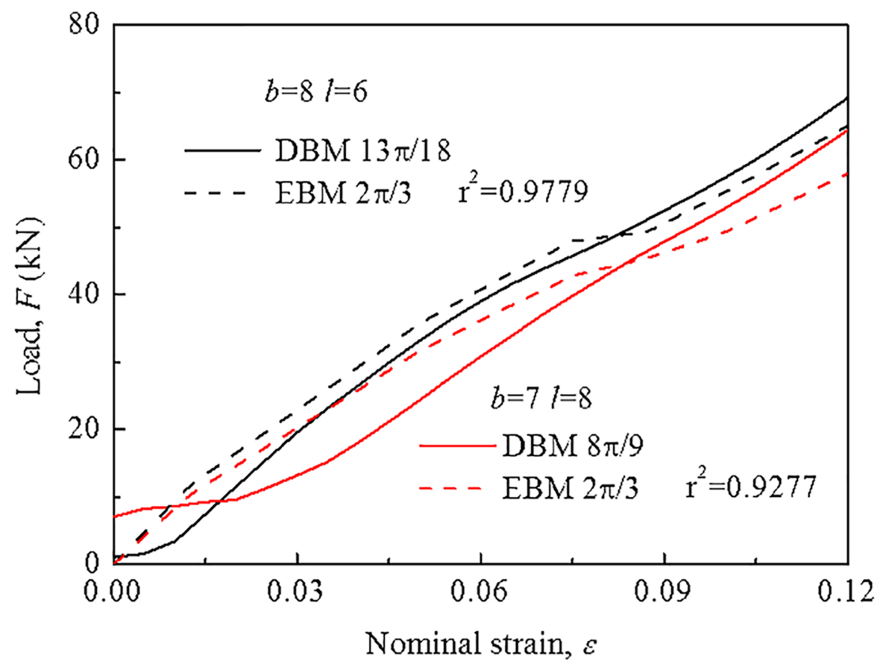


Fig 13. Validation for asymmetrical packing modes. Validation for predicting mechanical behavior of the module neglecting load plateau stage for asymmetrical packing modes by the EBM model for hexagonal dense packing.

<https://doi.org/10.1371/journal.pone.0181882.g013>

boundary condition was applied on it to acquire the homogenized mechanical properties. The experiments and corresponding DBM model were performed to validate the proposed homogenized EBM model under constrained compression loading conditions. For the cubic dense packing mode, the EBM model can well predict the mechanical behavior with length scale up to 15×15 and 15% deformation. For the hexagonal dense packing mode, the revised EBM model based on the packing density can represent well the mechanical properties of the module in the range of 12% deformation under different sizes. For asymmetrical packing modes where the structure of the module is unstable, after removing the load plateau stage that was caused by the relative motion of individual cells, the mechanical behavior of the module can be predicted well by the EBM model for hexagonal dense packing with the same size. Therefore, the homogenized modeling method is widely applicable for different packing modes.

Acknowledgments

This work is financially supported by the National Science Foundation of China under Grants No. 51605032, the National Science Foundation of Beijing under Grant No. 3174052 and the Fundamental Research Funds for the Central Universities No. 2017ZY31.

Author Contributions

Conceptualization: Liang Tang.

Data curation: Liang Tang, Jinjie Zhang.

Formal analysis: Liang Tang, Jinjie Zhang, Pengle Cheng.

Funding acquisition: Liang Tang.

Investigation: Liang Tang, Jinjie Zhang.

Methodology: Liang Tang.

Project administration: Liang Tang.

Resources: Liang Tang.

Software: Liang Tang.

Supervision: Liang Tang, Pengle Cheng.

Validation: Liang Tang.

Visualization: Jinjie Zhang.

Writing – original draft: Liang Tang.

Writing – review & editing: Jinjie Zhang, Pengle Cheng.

References

1. Wang D, Zamel N, Jiao K, Zhou Y, Yu S, Du Q, et al. Life cycle analysis of internal combustion engine, electric and fuel cell vehicles for China. *Energy*. 2013; 59:402–12.
2. Chan CK, Peng H, Liu G, Mcllwraith K, Zhang XF, Huggins RA, et al. High-performance lithium battery anodes using silicon nanowires. *Nat Nano*. 2008; 3(1):31–5.
3. Kang B, Ceder G. Battery materials for ultrafast charging and discharging. *Nature*. 2009; 458(7235):190–3. <https://doi.org/10.1038/nature07853> PMID: 19279634
4. Vikström H, Davidsson S, Höök M. Lithium availability and future production outlooks. *Applied Energy*. 2013; 110:252–66.
5. Zhou Y, Wang M, Hao H. Plug-in electric vehicle market penetration and incentives: a global review. *Mitigation and Adaptation Strategies for Global Change*. 2015; 20(5):777–95.

6. Hu X, Zou Y, Yang Y. Greener plug-in hybrid electric vehicles incorporating renewable energy and rapid system optimization. *Energy*. 2016; 111:971–80.
7. Song MK, Zhang Y, Cairns EJ. A long-life, high-rate lithium/sulfur cell: a multifaceted approach to enhancing cell performance. *Nano Letters*. 2013; 13(12):5891–9. <https://doi.org/10.1021/nl402793z> PMID: 24219588
8. Hu X, Jiang J, Bo E, Cao D. Advanced Power-Source Integration in Hybrid Electric Vehicles: Multicriteria Optimization Approach. *IEEE Transactions on Industrial Electronics*. 2015; 62(12):7847–58.
9. Hu X, Moura SJ, Murgovski N, Bo E, Cao D. Integrated Optimization of Battery Sizing, Charging, and Power Management in Plug-In Hybrid Electric Vehicles. *IEEE Transactions on Control Systems Technology*. 2016; 24(3):1036–43.
10. Hu X, Martinez CM, Yang Y. Charging, power management, and battery degradation mitigation in plug-in hybrid electric vehicles: A unified cost-optimal approach. *Mechanical Systems & Signal Processing*. 2017; 87:4–16.
11. Sun F, Hu X, Yuan Z, Li S. Adaptive unscented Kalman filtering for state of charge estimation of a lithium-ion battery for electric vehicles. *Energy*. 2011; 36(5):3531–40.
12. Hu X, Jiang J, Cao D, Bo E. Battery Health Prognosis for Electric Vehicles Using Sample Entropy and Sparse Bayesian Predictive Modeling. *IEEE Transactions on Industrial Electronics*. 2016; 63(4):2645–56.
13. Zheng L, Zhang L, Zhu J, Wang G, Jiang J. Co-estimation of state-of-charge, capacity and resistance for lithium-ion batteries based on a high-fidelity electrochemical model. *Applied Energy*. 2016; 180:424–34.
14. Zou C, Manzie C, Nestic D, Kallapur AG. Multi-time-scale observer design for state-of-charge and state-of-health of a lithium-ion battery. *Journal of Power Sources*. 2016; 335:121–30.
15. Xu J, Wu Y, Yin S. Investigation of effects of design parameters on the internal short-circuit in cylindrical lithium-ion batteries. *RSC Adv*. 2017; 7(24):14360–71. <https://doi.org/10.1039/c6ra27892b>
16. Zou C, Manzie C, Nešić D. A Framework for Simplification of PDE-Based Lithium-Ion Battery Models. *IEEE Transactions on Control Systems Technology*. 2016; 24(5):1594–609.
17. Lars H, Markus H. Lithium Ion Batteries for Hybrid and Electric Vehicles—Risks, Requirements and Solutions Out of the Crash Safety Point of View. 2011:11–0269.
18. Dai H, Wei X, Sun Z, Wang D. A novel dual-inductor based charge equalizer for traction battery cells of electric vehicles. *International Journal of Electrical Power & Energy Systems*. 2015; 67:627–38.
19. Wang Z, Liu P, Cui J, Xi Y, Zhang L, Wang Z, et al. Research on Quantitative Models of Electric Vehicle Charging Stations Based on Principle of Energy Equivalence. *Mathematical Problems in Engineering*. 2013; 69(3):831–42.
20. Sahraei E, Campbell J, Wierzbicki T. Modeling and short circuit detection of 18650 Li-ion cells under mechanical abuse conditions. *Journal of Power Sources*. 2012; 220:360–72. <https://doi.org/10.1016/j.jpowsour.2012.07.057>
21. Xu J, Wang L, Guan J, Yin S. Coupled effect of strain rate and solvent on dynamic mechanical behaviors of separators in lithium ion batteries. *Materials & Design*. 2016; 95:319–28. <https://doi.org/10.1016/j.matdes.2016.01.082>
22. Lai W-J, Ali MY, Pan J. Mechanical behavior of representative volume elements of lithium-ion battery modules under various loading conditions. *Journal of Power Sources*. 2014; 248:789–808. <https://doi.org/10.1016/j.jpowsour.2013.09.128>
23. Greve L, Fehrenbach C. Mechanical testing and macro-mechanical finite element simulation of the deformation, fracture, and short circuit initiation of cylindrical Lithium ion battery cells. *Journal of Power Sources*. 2012; 214:377–85. <https://doi.org/10.1016/j.jpowsour.2012.04.055>
24. Sahraei E, Hill R, Wierzbicki T. Calibration and finite element simulation of pouch lithium-ion batteries for mechanical integrity. *Journal of Power Sources*. 2012; 201:307–21. <https://doi.org/10.1016/j.jpowsour.2011.10.094>
25. Wierzbicki T, Sahraei E. Homogenized mechanical properties for the jellyroll of cylindrical Lithium-ion cells. *Journal of Power Sources*. 2013; 241:467–76. <https://doi.org/10.1016/j.jpowsour.2013.04.135>
26. Xu J, Liu B, Wang X, Hu D. Computational model of 18650 lithium-ion battery with coupled strain rate and SOC dependencies. *Applied Energy*. 2016; 172:180–9. <https://doi.org/10.1016/j.apenergy.2016.03.108>
27. Xu J, Liu B, Wang L, Shang S. Dynamic mechanical integrity of cylindrical lithium-ion battery cell upon crushing. *Engineering Failure Analysis*. 2015; 53:97–110. <https://doi.org/10.1016/j.engfailanal.2015.03.025>

28. Xu J, Liu B, Hu D. State of Charge Dependent Mechanical Integrity Behavior of 18650 Lithium-ion Batteries. *Sci Rep.* 2016; 6:21829. doi: [10.1038/srep21829](https://doi.org/10.1038/srep21829). PMID: [26911922](https://pubmed.ncbi.nlm.nih.gov/26911922/); PubMed Central PMCID: PMC4766446.
29. Sahraei E, Wierzbicki T, Hill R, Luo M. Crash Safety of Lithium-Ion Batteries Towards Development of a Computational Model. *Sae Technical Papers.* 2010.
30. Kukreja J, Nguyen T, Siegmund T, Chen W, Tsutsui W, Balakrishnan K, et al. Crash analysis of a conceptual electric vehicle with a damage tolerant battery pack. *Extreme Mechanics Letters.* 2016; 9:371–8. <https://doi.org/10.1016/j.eml.2016.05.004>
31. Ali MY, Lai W-J, Pan J. Computational models for simulation of a lithium-ion battery module specimen under punch indentation. *Journal of Power Sources.* 2015; 273:448–59. <https://doi.org/10.1016/j.jpowsour.2014.09.072>
32. Li S. On the unit cell for micromechanical analysis of fibre-reinforced composites. *Proceedings of the Royal Society A.* 1999; 455(1983):815–38.
33. Li S. General unit cells for micromechanical analyses of unidirectional composites. *Composites Part A Applied Science & Manufacturing.* 2001; 32(6):815–26.
34. Li S. Boundary conditions for unit cells from periodic microstructures and their implications. *Composites Science and Technology.* 2008; 68(9):1962–74. <https://doi.org/10.1016/j.compscitech.2007.03.035>
35. Xia Z, Zhang Y, Ellyin F. A unified periodical boundary conditions for representative volume elements of composites and applications. *International Journal of Solids and Structures.* 2003; 40(8):1907–21. [https://doi.org/10.1016/s0020-7683\(03\)00024-6](https://doi.org/10.1016/s0020-7683(03)00024-6)